


Antiferromagnetic Spin Orientation and Magnetic Domain Structure in Epitaxially Grown MnN Studied Using Optical Second-Harmonic Generation

Joongwon Lee^{1,*}, Zexuan Zhang,^{1,†} Huili (Grace) Xing,^{1,2} Debdeep Jena,^{1,2} and Farhan Rana¹

¹*School of Electrical and Computer Engineering, Cornell University, Ithaca, New York 14853, USA*

²*Department of Materials Science and Engineering, Cornell University, Ithaca, New York 14853, USA*

 (Received 4 April 2022; revised 3 August 2022; accepted 12 August 2022; published 8 September 2022)

MnN is a centrosymmetric collinear antiferromagnet belonging to the transition-metal-nitride family with a high Néel temperature (660 K), a low anisotropy field, and a large magnetic moment ($3.3\mu_B$ per Mn atom). Despite several recent experimental and theoretical studies, the spin symmetry (magnetic point group) and magnetic domain structure of the material remain unknown. In this work, we use optical second-harmonic generation (SHG) to study the magnetic structure of thin epitaxially grown single-crystal (001) MnN films. Our work shows that spin moments in MnN are tilted away from the [001] direction and the components of the spin moments in the (001) plane are aligned along one of the two possible in-plane symmetry axes ([100] or [110]), resulting in a magnetic-point-group symmetry of $2/m1'$. Our work rules out magnetic-point-group symmetries $4/mmm1'$ and $mmm1'$ that have been previously discussed in the literature. Four different spin domains consistent with the $2/m1'$ magnetic-point-group symmetry are possible in MnN. A statistical model based on the observed variations in the polarization-dependent intensity of the second-harmonic signal collected over large sample areas puts an upper bound of $0.65\ \mu\text{m}$ on the mean domain size. Our results show that SHG can be used to probe the magnetic order in metallic antiferromagnets. This work is expected to contribute to the recent efforts in using antiferromagnets for spintronic applications.

DOI: [10.1103/PhysRevApplied.18.034020](https://doi.org/10.1103/PhysRevApplied.18.034020)

I. INTRODUCTION

Antiferromagnetic (AF) materials have attracted considerable attention recently due to their potential for applications in spintronics [1,2]. The transition-metal nitrides are particularly interesting in this context because of the extensive range of electronic and magnetic properties that they display [3]. Mn-containing nitrides are especially interesting, because they form a variety of stoichiometric phases with Mn ions in various valence states. Among these phases one finds both antiferromagnets and ferrimagnets [4–9]. The diversity of magnetic orders, combined with the ability to epitaxially grow high-quality single-crystal films [10], makes Mn nitrides attractive for spintronics [11,12].

Spin-torque switching of the Néel order has been reported for several metallic and insulating AF materials [13–17]. Recently, electrical spin-torque switching has also been reported for MnN stacked with spin Hall metal Pt [12]. In many of these experiments, the electrical read-out schemes to detect the Néel order and its switching are weak. Various optical, x-ray, and thermal schemes have been proposed and used to investigate the Néel order [18–21]. Linear optical techniques, such as Faraday and Kerr rotation or linear and circular dichroism, do not

generally work in fully compensated AF materials other than in special cases where dc electric (or magnetic) fields can be applied to generate a linear optical response in AF materials lacking inversion (or time-reversal) symmetry [22] or where the magnetic order in the AF material is strongly coupled to the crystal structure and lattice strain [19,20,23]. Nonlinear optical techniques, and SHG in particular, have been shown to be sensitive to the Néel order and magnetic domain structure in AF materials [24,25] as a result of the magnetic dipole and electric quadrupole transitions in these materials. In this work, we use SHG to determine the magnetic-point-group symmetry and magnetic domain structure of epitaxially grown θ -phase MnN films.

θ -phase MnN has a tetragonally distorted rock-salt crystal structure. The Mn spin moments within a (001) plane are known to be aligned ferromagnetically and they are antiferromagnetically aligned in different (001) planes [4–9] [see Fig. 1(a)]. The exact orientation of the spin moments (and the magnetic point group) remains uncertain. Neutron diffraction studies have yielded conflicting results. Spins pointing within the (001) plane ($mmm1'$ magnetic-point-group symmetry) have been reported by Suzuki *et al.* [4] and spins pointing in a direction tilted 67° out of the (001) plane ($2/m1'$ symmetry) have been reported by Leineweber *et al.* [5]. In addition, spins pointing along the [001] direction ($4/mmm1'$ symmetry)

*j13755@cornell.edu

†zz523@cornell.edu

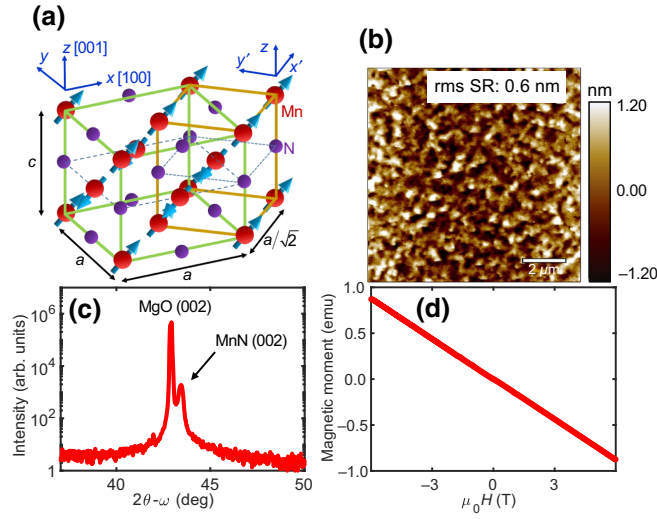


FIG. 1. (a) The unit cells and magnetic ordering in MnN ($2/m1'$ symmetry). Both the fcc (unprimed axes) and bcc (primed axes) unit cells of the tetragonal crystal are depicted. (b) An AFM scan of the surface of epitaxially grown (001) MnN. The rms surface roughness (SR) is 0.6 nm. (c) The x-ray diffraction pattern of epitaxially grown MnN. (d) A room-temperature out-of-plane magnetic hysteresis study of a 500-nm-thick MnN sample (grown on (001) MgO).

have been predicted theoretically [26] and have also been reported in measurements done at high temperatures [5]. MnN unit cells with different magnetic-point-group symmetries are depicted in Figs. 2(a)–2(c). The four Néel vectors \vec{L} corresponding to the four different magnetic domains consistent with the $2/m1'$ symmetry are shown in Fig. 2(d). Note that the magnetic-point-group symmetry remains unchanged if the components of the spin moments in the (001) plane are aligned along either one of the two sets of symmetry axes, $\langle 100 \rangle$ and $\langle 110 \rangle$. In specifying the magnetic point groups, we use the convention that in an antiferromagnetically ordered periodic crystal, the magnetic point group consists of all crystal-point-group operations, together with the time-inversion operation, that leave the crystal (including the magnetic order) invariant to within a translation [27]. Mn:N ratios in the 6:5.85 to 6:5.95 range have been reported for θ -MnN in the literature [5]. However, no long-range order or structure has been found corresponding to the missing nitrogen atoms [5]. The nitrogen vacancies are thought to stabilize the rock-salt structure over the competing zinc-blende structure [9].

II. MATERIAL GROWTH AND CHARACTERIZATION

The MnN samples used in this study are grown using plasma-assisted molecular-beam epitaxy (MBE) on (001) MgO substrates. A high-purity elemental Mn effusion cell

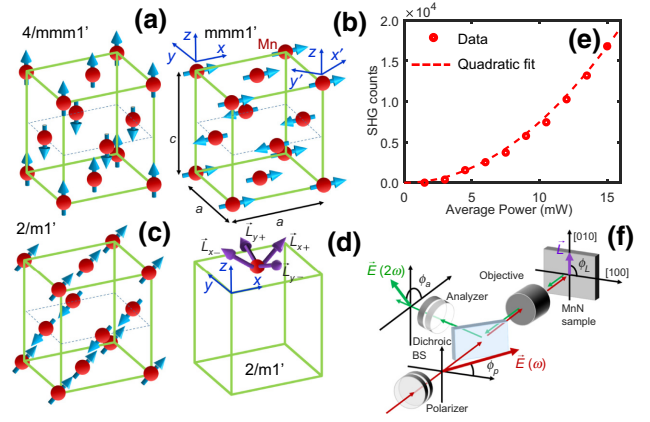


FIG. 2. A MnN unit cell with different spin structures corresponding to (a) $4/mmm1'$, (b) $mmm1'$, and (c) $2/m1'$ magnetic-point-group symmetries. (d) The Néel vectors \vec{L} for different magnetic domains consistent with $2/m1'$ symmetry. (e) The measured SH signal from a MnN sample, showing a quadratic dependence on the pump power ($T = 300$ K). (f) The experimental setup for measuring SHG. ϕ_p , ϕ_a , and ϕ_L are the angles of the polarizer, analyzer, and the in-plane component of the Néel vector \vec{L} with respect to the crystal [100] axis.

supplies the metal flux and ultrahigh-purity nitrogen gas is supplied through a plasma source. Growth is carried out at a thermal couple temperature of 425 °C. A Mn beam equivalent pressure (BEP) of 10^{-7} Torr and a nitrogen plasma operating at 450 W with a N_2 gas flow rate of 3.2 sccm are used for MnN layer deposition. A symmetric $2\theta/\omega$ x-ray diffraction (XRD) scan is shown in Fig. 1(c). The observation of only integer orders of MnN (002) and MgO (002) peaks suggests that the MnN layers are single crystal, with the c -axis out of plane, and have no appreciable alien-phase inclusion. Atomic-force-microscopy (AFM) measurements [Fig. 1(b)] on a 500-nm-thick MnN sample reveal a smooth surface with 0.6-nm root-mean-square (rms) roughness. A resistivity of $90 \mu\Omega$ cm, a carrier concentration of $4 \times 10^{21} \text{ cm}^{-3}$, and a carrier mobility of $17 \text{ cm}^2 \text{ V}^{-1} \text{ s}^{-1}$ obtained from Hall measurements reveal metallic properties. The sign of the charge of the charge carriers is found to be negative, consistent with the computed electronic band structure of antiferromagnetic MnN [7]. Vibrating sample magnetometry (VSM) with the magnetic field applied in the out-of-plane direction exhibits no hysteresis loop up to 6 T [Fig. 1(d)], ruling out the inclusion of ferrimagnetic precipitates, such as Mn_4N , in the films.

III. OPTICAL SECOND-HARMONIC GENERATION

Second-harmonic (SH) measurements are conducted using an ytterbium laser with a 1032-nm center wavelength, a 150-fs pulse width and a 100-MHz repetition rate. All measurements are performed with 6 mW average

power at room temperature. To minimize sample heating, the pump is mechanically chopped at 100 Hz with 30% duty cycle. The pump is focused down to an $2.5\text{-}\mu\text{m}$ -diameter optical spot on the sample at normal incidence. The SH signal is collected in a reflection geometry. The quadratic dependence of the collected SH intensity on the pump power is confirmed [Fig. 2(e)]. The polarization angles of the incident pump (polarizer angle) and the collected SH signal (analyzer angle) are selected using a set of half-wave plates and Glan-Thompson polarizers [see Fig. 2(f)]. Figure 3 shows the SHG signal dependence on the polarizer and analyzer angles in eight different configurations. First, the polarizer is fixed at (a) 0° , (b) -45° , (c) -90° , and (d) -135° while the analyzer is rotated through 360° . Second, the polarizer is rotated through 360° while the analyzer is fixed at (e) 0° , (f) -45° , (g) -90° , and (h) -135° . All angles indicated are with respect to the $[100]$ axis. The SH data are collected at a large number of points in a $100\text{-}\mu\text{m}^2$ -area grid on the samples. Two important features visible in the data in Fig. 3 are as follows: (i) the SH measured is always polarized perpendicular to the pump; and (ii) the peak SH intensity is independent of the pump polarization. The data shown in Fig. 3 are obtained from a 500-nm -thick MnN sample. Thinner samples exhibit similar features. In the sections that follow, we analyze these results, propose a model to explain the observed features, and relate the observations to the magnetic structure of the MnN films.

IV. THEORETICAL MODELING AND DISCUSSION

Although the centrosymmetric structure of MnN does not allow SHG (of pure electric dipole origin) in the bulk, broken-inversion symmetry at the surface could generate a strong electric dipole SH signal that can be stronger than the bulk SH signal. We first note that the (001) surface of MnN has an in-plane C_{4v} symmetry (in the absence of any surface magnetic order), which does not allow surface-normal electric dipole SHG. To make the case stronger against the measured SH signal coming from the surface and rule out the possibility of the surface magnetic order contributing to the measured SH signal, we characterize samples with different thicknesses. Thicker samples generate more SH signal than thinner samples. The dependence of the measured SH intensity on the sample thickness d is fitted with the approximate relation $1 - \exp(-2\alpha(\omega)d - \alpha(2\omega)d)$ with the combined fundamental and SH loss, $2\alpha(\omega) + \alpha(2\omega)$, equal to 7.5×10^7 1/m. For example, a 20-nm -thick sample generates, on average, approximately 15% more SH signal intensity than a 15-nm -thick sample. We, therefore, rule out any significant surface contribution to the measured SH signals. The presence of a large number of nitrogen vacancies in θ -MnN, as reported previously [5], can contribute to the breaking of local inversion

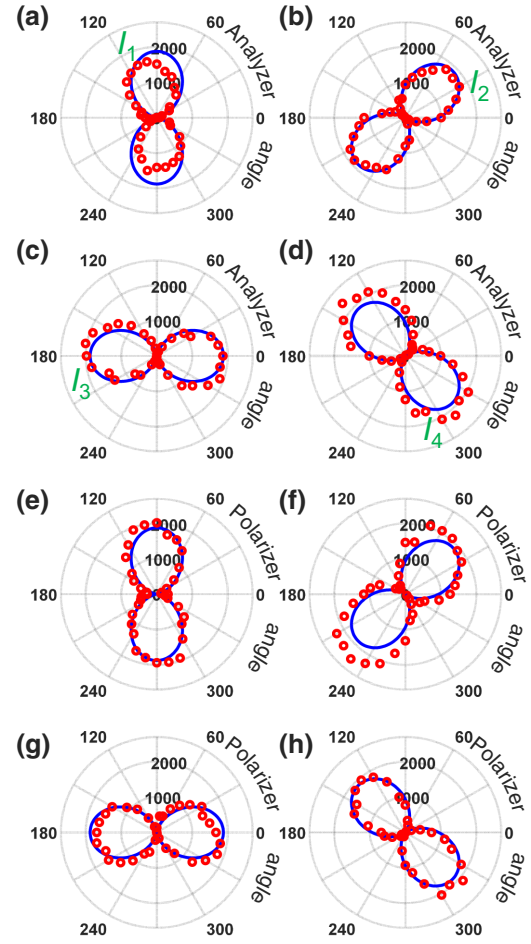


FIG. 3. SH photon counts plotted as a function of the analyzer angle while the polarizer angle is fixed at (a) 0° , (b) -45° , (c) -90° , and (d) -135° . Also shown are the SH counts as a function of the polarizer angle (α) while the analyzer angle (β) is fixed at (e) 0° , (f) -45° , (g) -90° , and (h) -135° . Experimental data from a single representative spot are shown in red dots. The data shown in the figure are obtained from a 500-nm -thick sample. Thinner samples exhibit similar features. Results from our theoretical model, discussed in the text, are also shown (solid lines). I_1 , I_2 , I_3 , and I_4 are the peak intensities.

symmetry in the bulk. However, given the lack of any long-range order or structure in the positions of the missing nitrogen atoms [5], inversion symmetry is expected to remain a good symmetry (on the scale of the optical wavelength) as far as SHG is concerned.

We assume that the Néel vector in the bulk is $\vec{L} = \vec{m}_1 - \vec{m}_2$ and its component in the (001) plane is \vec{L}_\parallel . SHG in the centrosymmetric bulk due to magnetic dipole and electric quadrupole transitions can be expressed as

$$P_i(2\omega) = \{\chi_{ijk}^{em} + \gamma_{ijk}^{em}(\vec{L})\}E_j(\omega)H_k(\omega) + \{\chi_{ijkl}^{eee} + \gamma_{ijkl}^{eee}(\vec{L})\}E_j(\omega)\partial_l E_k(\omega). \quad (1)$$

Here, the first two terms describe a second-order process in which one of the intermediate transitions is of magnetic dipole origin [25] and the next two terms describe a process in which one of the intermediate transitions is of electric quadrupole origin. The rationale for selecting magnetic dipole and electric quadrupole intermediate transitions are discussed later. When allowed, both magnetic dipole and electric quadrupole transitions can be of comparable strengths in transition-metal ions and compounds [28]. The components of the susceptibility tensors that do not vanish as a consequence of the crystal and magnetic symmetries can be determined as follows. χ_{ijk}^{em} and χ_{ijk}^{ee} do not depend on the magnetic order and their nonzero components are determined by the 4/mmm structural symmetry of the crystal. Both these tensors have no nonzero components that can contribute to SHG in the surface-normal direction. The nonzero components of γ_{ijk}^{em} and γ_{ijk}^{ee} are determined by the magnetic-point-group symmetry of the crystal. Assuming a surface-normal direction of the pump, in the case of both 4/mmm1' and mmm1' magnetic-point-group symmetries [Figs. 2(a) and 2(b)], γ_{ijk}^{em} and γ_{ijk}^{ee} have no nonzero components that can generate a SH signal in the surface-normal direction. If the magnetic-point-group symmetry is 2/m1' [Fig. 2(c)], both γ_{ijk}^{em} and γ_{ijk}^{ee} have four nonzero components that can contribute to a SH signal in the surface-normal direction. Assuming that \vec{L}_{\parallel} is along the [100] direction, these components are: (i) γ_{yxx}^{em} , γ_{xyx}^{em} , γ_{xyy}^{em} , and γ_{yyx}^{em} and (ii) γ_{xyyz}^{ee} , γ_{xyzy}^{ee} , γ_{xxz}^{ee} , and γ_{yyz}^{ee} . If \vec{L}_{\parallel} is along any other direction (e.g., [110] or [010]), the nonzero tensor components can be obtained by a rotation of the coordinates [29]. The analysis here shows that nonzero susceptibility-tensor components that contribute to the SH signal in the surface-normal direction result from the reduced symmetry generated by the magnetic order and are therefore a good probe of the magnetic order. We also experimentally correlate the magnetic order to the SH signal in the temperature dependent results presented in the Appendix.

We should point out that symmetry in many cases allows nonzero tensor components that generate a surface-normal polarization $P_z(2\omega)$. Although $P_z(2\omega)$ does not contribute to SH in the strictly surface-normal direction, it can contribute to SH at nonzero angles from the surface normal. The amount of SH signal generated by $P_z(2\omega)$ that is collected in a surface-normal reflection-based measurement setup such as ours is determined by the numerical aperture (NA) of the objective. SH generated by $P_z(2\omega)$ itself exhibits an intensity that is independent of the analyzer angle. Interference with other in-plane polarization components could result in asymmetric lobes in the patterns displayed in Fig. 3. However, in our experiments, the use of collection objectives with different numerical apertures (NAs in the 0.1–0.6 range) result in no discernible changes in the patterns displayed in Fig. 3. Note also that in the case of 4/mmm1' and mmm1' magnetic-point-group

symmetries, any contribution to the SH signal from $P_z(2\omega)$ would have resulted in the SH intensity being independent of the analyzer angle, in disagreement with the measured results in Fig. 3. Next, we show that the nonzero components of γ_{ijk}^{em} and γ_{ijk}^{ee} , assuming 2/m1' magnetic-point-group symmetry, can explain all our SH data provided that a statistical mixture of domains is assumed within the pump spot size.

We first focus on the tensor γ_{ijk}^{em} and assume that \vec{L}_{\parallel} is along the [100] axis. Since the measured SH is always perpendicular to the pump, we require that $\gamma_{xxy}^{em} = \gamma_{yyx}^{em} = 0$ and $\gamma_{yxx}^{em} = -\gamma_{xyx}^{em}$. We are then left with only one independent component for the γ_{ijk}^{em} tensor that can contribute to surface-normal SHG. Assuming a single magnetic domain, if the angles with respect to the [100] axis of \vec{L}_{\parallel} , the analyzer, and the polarizer are ϕ_L , ϕ_a , and ϕ_p , respectively, then the SH intensity in the surface-normal direction comes out to be proportional to

$$\sin^2(\phi_a - \phi_p) \sin^2(\phi_L - \phi_p). \quad (2)$$

The SH signal obtained above exhibits a single lobe polarized perpendicular to the pump and the SH intensity goes to zero when the pump is polarized parallel to \vec{L}_{\parallel} . In principle, SHG can therefore be used to detect the orientation of the in-plane component \vec{L}_{\parallel} of the Néel vector provided that the sample consists of a single domain. In experiments, the SH signal is always found to be polarized perpendicular to the pump, consistent with the model [see Figs. 3(a)–3(d)]. However, the peak SH intensity is seen to be independent of the pump polarization. The experimental results can be explained by assuming many magnetic domains within the pump optical spot size of 2.5 μm . The Néel vectors of the four possible magnetic domains consistent with 2/m1' magnetic-point-group symmetry are shown in Fig. 2(d) and correspond to ϕ_L values of 0, $\pm\pi/2$, and π . We assume, for simplicity, that the sizes of individual domains are much smaller than the pump spot size and the SH wavelength. This assumption is relaxed later when we present results from the computational model. We assume that the pump is polarized at an angle ϕ_p with respect to the sample [100] axis. The far-field SH intensity $I_{SH}(\phi_a, \phi_p, \theta, \phi)$ in the (θ, ϕ) direction, collected by the objective, and after passing through the analyzer fixed at angle ϕ_a , can be obtained by coherently superposing the SH field emitted by all the domains within the pump spot size. The spherical coordinate angles θ (ϕ) are measured with respect to the [001] ([100]) axis. The result, for small values of θ , can be written as

$$\begin{aligned} & I_{SH}(\phi_a, \phi_p, \theta, \phi) \\ & \propto \sin^2(\phi_a - \phi_p) \sum_{m,n} \sin(\phi_L^m - \phi_p) \\ & \quad \times \sin(\phi_L^n - \phi_p) e^{-ik \sin \theta [(x^m - x^n) \cos \phi + (y^m - y^n) \sin \phi]}. \quad (3) \end{aligned}$$

The sum over m/n is over all the N domains located at coordinates $(x^{m/n}, y^{m/n})$ in the sample within the pump spot size. If the domains are much smaller than the pump spot size and the SH wavelength, the terms in this sum interfere with each other strongly and the sum is then dominated by the diagonal terms for which $m = n$. Keeping only these terms gives the approximate expression

$$I_{SH}(\phi_a, \phi_p, \theta, \phi) \propto \sin^2(\phi_a - \phi_p) \sum_m \sin^2(\phi_L^m - \phi_p) \\ \approx \frac{N}{2} \sin^2(\phi_a - \phi_p). \quad (4)$$

The above result corresponds to a single-lobe SH signal polarized perpendicular to the pump, the peak intensity of which is independent of the pump polarization. The expression in Eq. (4), plotted as a solid line in Figs. 3(a)–3(h), is seen to match the SH data very well for all polarizer and analyzer angles. Note that if \vec{L}_{\parallel} is assumed to be along the $\langle 110 \rangle$ direction (which is also consistent with a $2/m1'$ magnetic point group) and ϕ_L has values $\pm\pi/4$ and $\pm 3\pi/4$, the result in Eq. (4) remains unchanged. Therefore, if the magnetic domains are much smaller than pump spot size and the SH wavelength, our measurements cannot distinguish between $\langle 100 \rangle$ and $\langle 110 \rangle$ orientations of \vec{L}_{\parallel} .

We make two remarks about the analysis presented above. First, in actual experiments, the SH signal is collected within a cone determined by the NA of the collection objective and the values of θ for which the SH signal is recorded are not always very small. Second, suppose that the domain sizes increase from very small values to sizes comparable to the pump spot size and the SH optical wavelength ($0.5 \mu\text{m}$). One then ought to observe larger fluctuations in the measured SH intensities as one collects SH signal from different spatial spots on the sample. This is noteworthy because the strength of the measured fluctuations in the SH data collected from a large number of spots on the sample can be used to place an upper limit on the domain sizes in the sample. To model this phenomenon more carefully, we develop a finite-element computational model in which we divide the sample area within the pump spot size into different square-shaped magnetic domains of a given size and the divided each domain further into smaller pixels of size 10 nm. We then compute the SH far field from the bulk SH polarization $P(2\omega)$ in every pixel. The SH field within the collection light cone (the cone angle determined by the NA of the objective is assumed to be 0.5) is collimated and squared to obtain the SH intensity. The SH intensity thus obtained is ensemble averaged. A typical ensemble consists of 500 different magnetic domain configuration within the pump spot size, corresponding to ϕ_L values of 0, $\pm\pi/2$, and π . The results obtained are shown in Fig. 4, which plots the normalized average [Fig. 4(a)] and the normalized variance [Fig. 4(b)]

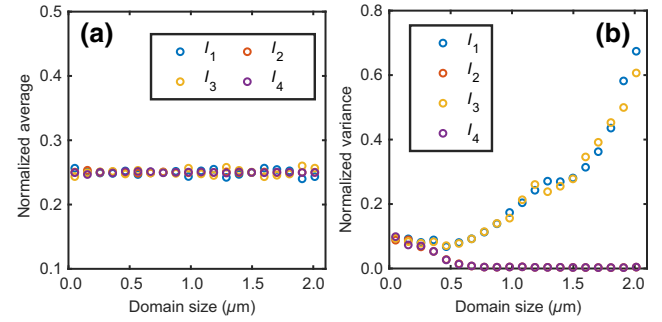


FIG. 4. The calculated (a) normalized average and (b) normalized variance of the peak SH intensities I_1 , I_2 , I_3 , and I_4 (for different pump polarizations; see Fig. 3), plotted as a function of the magnetic domain size.

of the peak SH intensities I_1 , I_2 , I_3 , and I_4 (for different pump polarizations, see Fig. 3) as a function of the magnetic domain size. The normalized average $e[I_j]$ and variance $v[I_j]$ are defined as $e[I_j] = E[I_j] / \sum_j E[I_j]$ and $v[I_j] = (E[I_j^2] - E[I_j]^2) / E[I_j]^2$. In the limit of very large domain sizes, one expects $v[I_{2/4}]$ to go to zero and $v[I_{1/3}]$ to approach unity, given the two nonzero components of the susceptibility tensor $\gamma_{yxx}^{eem} = -\gamma_{xyx}^{eem}$. The computation shows that the fluctuations in $I_{1/3}$ become large once the domain sizes exceed the SH wavelength ($0.5 \mu\text{m}$). In experiments, ensemble averaging is performed by recording the SH signal from different spots on the sample. The experimental value of $e[I_j]$ is approximately 0.25 for all I_j , in very good agreement with the computational model. The experimental values of $v[I_j]$ are found to be smaller than .02 for all I_j . This value is slightly smaller than the smallest computed values for $v[I_{2/4}]$ of 0.04 and for $v[I_{1/3}]$ of 0.07 that occur for a domain size of approximately $0.45 \mu\text{m}$. This small discrepancy can be attributed to our use of the same domain shape and size in all ensembles. A more complex model that uses domains of slightly different shapes and sizes within the same ensemble would be closer to reality and is expected to reduce the computed variance in the limit of small domain sizes. The comparison between experiments and the model enables us to place a rough upper bound on the domain sizes in our samples of $0.65 \mu\text{m}$, given that the variances $v[I_{1/3}]$ become large for larger domain sizes. This procedure does not provide a tight upper bound.

Next, we focus on the nonzero components of the tensor γ_{ijkz}^{eee} that result from an electric quadrupole intermediate transition. The symmetry properties of γ_{ijkz}^{eee} are very similar to those of γ_{ijk}^{eem} and, quite remarkably, the assumptions $\gamma_{xxxz}^{eee} = \gamma_{yyxz}^{eee} = 0$ and $\gamma_{yxyz}^{eee} = -\gamma_{xyyz}^{eee}$ can explain our data just as well as the tensor γ_{ijk}^{eem} discussed above. To explore the origin of the SHG in our samples and possibly single

out one tensor responsible for the SHG, we look at the electron energy levels of d orbitals in Mn^{3+} ($3d^4$) in the MnN environment [30,31].

V. OPTICAL TRANSITIONS AND THE ORIGIN OF SH POLARIZATION

The bands near the Fermi energy in MnN are formed by weakly coupled d orbitals of adjacent Mn atoms. The nitrogen p orbitals in MnN have been found to be lower in energy [6,9]. It is therefore reasonable to assume that the selection rules for optical transitions can be determined from the symmetries of the energy levels of a Mn^{3+} ion in the tetragonal $4/mmm$ environment. Since the tetragonal distortion in MnN is small (the Mn—N bond length is 2.128 Å (2.095 Å) along the a -axis (c -axis) [8]), the local environment of each Mn atom can be approximated by the octahedral (O_h) group rather than the D_{4h} group without affecting the main results that follow. The lowest energy levels, and their symmetries, of Mn^{3+} in an octahedral environment are depicted in Fig. 5. The lowest occupied level has ${}^5\Gamma_3^+$ symmetry and in an octahedral environment ${}^5\Gamma_3^+ = \sum_{i=1}^5 \oplus \Gamma_i^+$. The magnetic dipole transition operator has the symmetry Γ_4^+ and since ${}^5\Gamma_3^+ \otimes \Gamma_4^+ = \Gamma_1^+ \oplus \Gamma_2^+ \oplus 2\Gamma_3^+ \oplus 4(\Gamma_4^+ \oplus \Gamma_5^+)$, magnetic dipole transitions are allowed between ${}^5\Gamma_3^+$ and all multiplets of the higher-energy ${}^5\Gamma_5^+$ level. The electric quadrupole transition operator has the symmetries Γ_5^+ (off-diagonal components) and Γ_3^+ (diagonal components). Also, since ${}^5\Gamma_3^+ \otimes \Gamma_5^+ = \Gamma_1^+ \oplus \Gamma_2^+ \oplus 2\Gamma_3^+ \oplus 4(\Gamma_4^+ \oplus \Gamma_5^+)$ and ${}^5\Gamma_3^+ \otimes \Gamma_3^+ = \Gamma_1^+ \oplus \Gamma_2^+ \oplus 3\Gamma_3^+ \oplus 2(\Gamma_4^+ \oplus \Gamma_5^+)$, electric quadrupole transitions are allowed between ${}^5\Gamma_3^+$ and all multiplets of the higher-energy ${}^5\Gamma_5^+$ level. Two possibilities behind the origin of SHG in MnN are depicted by the transition diagram in Fig. 5, which shows that one intermediate transition, involving the ground state, of the second-order nonlinear process is either of magnetic dipole or of electric quadrupole origin and the other two transitions, involving higher-energy states, are of electric dipole origin. The rationale for assigning transitions in this way is as follows. The transition from ${}^5\Gamma_3^+$ to ${}^3\Gamma_4^+$, and also transitions from ${}^5\Gamma_3^+$ and ${}^5\Gamma_5^+$ to other higher energy levels, require a spin flip and are expected to be weak. Since even spin-allowed magnetic dipole and electric quadrupole transitions are weak (much weaker than electric dipole transitions) [28], we expect the ${}^5\Gamma_3^+$ to ${}^5\Gamma_5^+$ spin-allowed transition to be of magnetic dipole or electric quadrupole character. Electric dipole transitions involving higher energy levels, although spin and dipole forbidden at the level of a single Mn ion, are expected to be strong and made possible by the larger coupling between d orbitals of adjacent Mn atoms at higher energies, enhanced d - p coupling at higher energies, and the presence of spin-orbit coupling [6,28,31]. Finally, since the pump and SHG photon energies in our experiments are approximately 1.2 eV and 2.4 eV, respectively, we do not

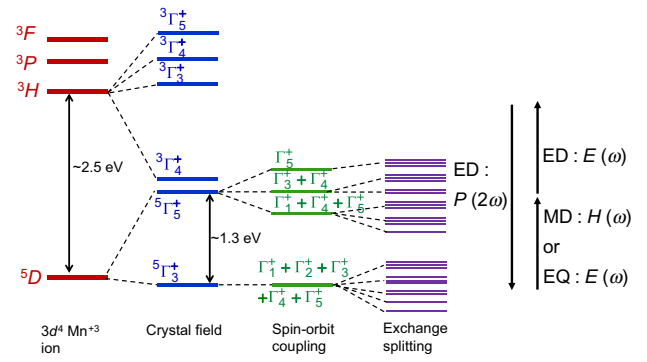


FIG. 5. The energy levels of Mn^{3+} in MnN [30,31]. Both magnetic dipole (MD) and electric quadrupole (EQ) transitions are allowed between the lowest-energy ${}^5\Gamma_3^+$ multiplets and the multiplets of the upper ${}^5\Gamma_5^+$ level. Energy-level splittings due to the small tetragonal distortion in MnN are ignored. The energy-level splittings shown are not drawn to scale. ED, electric dipole.

expect any one of the transitions contributing to SHG in our experiments to be fully resonant.

VI. CONCLUSIONS

In conclusion, the SHG measurement scheme is found to be sensitive to the antiferromagnetic order in MnN and enables the selection of $2/m1'$ as the magnetic-point-group symmetry of MnN from among other competing candidates. Our work shows that SHG can be used to place a loose upper bound on the domain sizes. Our work also shows that SHG can be used to probe the magnetic order in bulk metallic antiferromagnets. Previously, this technique has been used to probe the magnetic order in bulk insulating antiferromagnets [24,25]. We expect that in single-domain MnN samples, this technique can be used to detect the in-plane orientation of the Néel vector and also its switching in response to stimuli such as the spin-transfer torque [1,2,12]. Nonlinear optical techniques can thus play an important role in antiferromagnetic spintronics.

ACKNOWLEDGMENTS

This work was supported by the Cornell Center for Materials Research with funding from the National Science Foundation (NSF) Materials Research Science and Engineering Centers (MRSEC) program (DMR-1719875). We would like to acknowledge helpful discussions with Okan Koksals, Gregory D. Fuchs, and Daniel C. Ralph. We would like to thank Joseph Casamento for x-ray photoelectron spectroscopy measurements.

J.L. and Z.Z. contributed equally to this work. <pag/>

APPENDIX: TEMPERATURE DEPENDENCE OF THE SECOND-HARMONIC INTENSITY

In the discussion following Eq. (1), we argue that the only contributions to the measured SH intensity in the surface-normal direction can come from the components $\gamma_{ijk}^{eem}(\vec{L})$ and $\gamma_{ijkl}^{eee}(\vec{L})$ of the susceptibility tensor that explicitly depend on the Néel vector \vec{L} . Since in antiferromagnets the magnitudes of the Néel-vector components are temperature dependent [32], one would expect the measured SHG intensity to be temperature dependent as well. Figure 6 shows the measured SH intensity as a function of the temperature. The small spread in the data is attributed to thermal expansions or contractions in the sample mount inside the cryostat with temperature changes that are expected to result in a shift of the optical focus spot by tens of nanometers, and perhaps a few hundred nanometers, which are comparable to the domain sizes in the sample. The data shows that the SH intensity decreases as the temperature increases. Due to the limitations of our experimental setup, data beyond room temperature cannot be obtained.

To explain the data, we assume the simplest model, that in which the decrease in the sublattice magnetization is caused by excitation of the antiferromagnetic magnons [32]. If the magnons have a spin gap Δ , as is often the case in antiferromagnets with anisotropy [32], then for temperatures lower than $\Delta/(3k_B)$, the temperature dependence of the Néel vector is given as [33]

$$L_j(T) \propto \left[1 - Ae^{-\Delta/k_B T} \left(\frac{T}{T_N} \right)^{3/2} \right], \quad (\text{A1})$$

where A is a constant, and for temperatures higher than $\Delta/(3k_B)$ but smaller than $0.5T_N$, the temperature

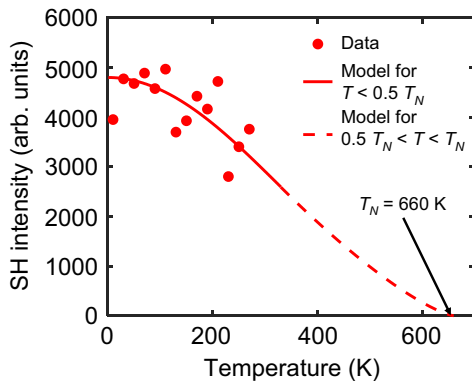


FIG. 6. The measured SH intensity (for polarizer and analyzer angles that yield the maximum SH intensity) for MnN, plotted as a function of the temperature T (circles). The solid and dashed lines show the fit obtained using the models discussed in the text, valid for $0 < T < 0.5T_N$ and $0.5T_N < T < T_N$, respectively.

dependence of the Néel vector is described by [32,33]

$$L_j(T) \propto \left[1 - B \left(\frac{T}{T_N} \right)^2 \right]. \quad (\text{A2})$$

Here, $B \approx 0.57$. Since the spin gap Δ is no larger than a few millielectronvolts in almost all metallic antiferromagnets, we expect the expression in Eq. (A2) to better describe the temperature dependence of our data for $10K < T < 0.5T_N$. For even higher temperatures, $0.5T_N < T < T_N$, the temperature dependence of $L_j(T)$ has been shown to be given by [34]

$$L_j(T) \propto \left[1 - \frac{T}{T_N} \right]^\beta, \quad (\text{A3})$$

where the critical exponent β is close to 1/3 [34]. To relate the temperature dependence of $\vec{L}(T)$ to the temperature dependence of the SH intensity, we proceed as follows. The tensors, $\gamma_{ijk}^{eem}(\vec{L})$ and $\gamma_{ijkl}^{eee}(\vec{L})$, can both be expanded as follows:

$$\gamma_{ijk}(\vec{L}) = \gamma_{ijk}^{(1)}L_r + \gamma_{ijk}^{(2)}L_rL_s + \dots \quad (\text{A4})$$

Since $\vec{L} \rightarrow -\vec{L}$ is a symmetry of the MnN crystal (up to a lattice translation), the first term in the above expansion that contributes to the SH intensity in MnN is the second term, with a quadratic dependence on the Néel-vector components. Ignoring Δ for simplicity (since Δ is expected to be very small), the temperature dependence of the SH intensity $I(T)$ in MnN, for $T < 0.5T_N$ ought to be

$$I(T) \approx I(T=0) \left[1 - B \left(\frac{T}{T_N} \right)^2 \right]^4. \quad (\text{A5})$$

The fit to our data obtained by using the above expression is shown by the solid line in Fig. 6. The fit assumes a Néel temperature T_N of 660 K. The data are seen to match the model very well for temperatures below room temperature. The decay of the SHG intensity with temperature as T^2 is expected to be valid for $T \ll T_N$ and our data are in agreement with this behavior.

- [1] T. Jungwirth, X. Marti, P. Wadley, and J. Wunderlich, Antiferromagnetic spintronics, *Nat. Nanotechnol.* **11**, 231 (2016).
- [2] V. Baltz, A. Manchon, M. Tsoi, T. Moriyama, T. Ono, and Y. Tserkovnyak, Antiferromagnetic spintronics, *Rev. Mod. Phys.* **90**, 015005 (2018).
- [3] D. A. Papaconstantopoulos, W. E. Pickett, B. M. Klein, and L. L. Boyer, Electronic properties of transition-metal nitrides: The group-V and group-VI nitrides VN, NbN, TaN, CrN, MoN, and WN, *Phys. Rev. B* **31**, 752 (1985).

- [4] K. Suzuki, Y. Yamaguchi, T. Kaneko, H. Yoshida, Y. Obi, H. Fujimori, and H. Morita, Neutron diffraction studies of the compounds MnN and FeN, *J. Phys. Soc. Jpn.* **70**, 1084 (2001).
- [5] A. Leineweber, R. Niewa, H. Jacobs, and W. Kockelmann, The manganese nitrides η -Mn₃N₂ and θ -Mn₆N_{5+x}: nuclear and magnetic structures, *J. Mater. Chem.* **10**, 2827 (2000).
- [6] B. R. Sahu and L. Kleinman, Theoretical study of electronic and magnetic properties of MnN, *Phys. Rev. B* **68**, 113101 (2003).
- [7] W. R. L. Lambrecht, M. Prikhodko, and M. S. Miao, Electronic structure and magnetic interactions in MnN and Mn₃N₂, *Phys. Rev. B* **68**, 174411 (2003).
- [8] S. Granville, B. J. Ruck, F. Budde, A. Koo, J. E. Downes, H. J. Trodahl, A. Bittar, N. Strickland, G. V. M. Williams, W. R. L. Lambrecht, T. Learmonth, K. E. Smith, V. J. Kennedy, A. Markwitz, and T. Schmitt, Optical conductivity and x-ray absorption and emission study of the band structure of MnN films, *Phys. Rev. B* **72**, 205127 (2005).
- [9] J. A. Chan, J. Z. Liu, H. Raebiger, S. Lany, and A. Zunger, Relative stability, electronic structure, and magnetism of MnN and (Ga, Mn)N alloys, *Phys. Rev. B* **78**, 184109 (2008).
- [10] D. Jena, R. Page, J. Casamento, P. Dang, J. Singhal, Z. Zhang, J. Wright, G. Khalsa, Y. Cho, and H. G. Xing, The new nitrides: Layered, ferroelectric, magnetic, metallic and superconducting nitrides to boost the GaN photonics and electronics eco-system, *Jpn. J. Appl. Phys.* **58**, SC0801 (2019).
- [11] P. Zilske, D. Graulich, M. Dunz, and M. Meinert, Giant perpendicular exchange bias with antiferromagnetic MnN, *Appl. Phys. Lett.* **110**, 192402 (2017).
- [12] M. Dunz, T. Matalla-Wagner, and M. Meinert, Spin-orbit torque induced electrical switching of antiferromagnetic MnN, *Phys. Rev. Res.* **2**, 013347 (2020).
- [13] K. Olejnik, V. Schuler, X. Marti, V. Novak, Z. Kaspar, P. Wadley, R. Campion, K. Edmonds, B. Gallagher, J. Garces, M. Baumgartner, P. Gambardella, and T. Jungwirth, Antiferromagnetic cumnas multi-level memory cell with micro-electronic compatibility, *Nat. Commun.* **8**, 15343 (2017).
- [14] S. Bodnar, L. Šmejkal, I. Turek, T. Jungwirth, O. Gomonay, J. Sinova, A. Sapozhnik, H. Elmers, M. Kläui, and M. Jourdan, Writing and reading antiferromagnetic Mn₂Au by Néel spin-orbit torques and large anisotropic magnetoresistance, *Nat. Commun.* **9**, 348 (2018).
- [15] X. Chen, R. Zarzuela, J. Zhang, C. Song, X. Zhou, G. Shi, F. Li, H. Zhou, W. Jiang, F. Pan, and Y. Tserkovnyak, Antidamping-Torque-Induced Switching in Biaxial Antiferromagnetic Insulators, *Phys. Rev. Lett.* **120**, 207204 (2018).
- [16] T. Moriyama, K. Oda, T. Ohkochi, M. Kimata, and T. Ono, Spin torque control of antiferromagnetic moments in NiO, *Sci. Rep.* **8**, 14167 (2018).
- [17] Y. Cheng, S. Yu, M. Zhu, J. Hwang, and F. Yang, Electrical Switching of Tristate Antiferromagnetic Néel Order in α -Fe₂O₃ Epitaxial Films, *Phys. Rev. Lett.* **124**, 027202 (2020).
- [18] I. Gray, T. Moriyama, N. Sivadas, G. Stiehl, J. Heron, R. Need, B. Kirby, D. Low, K. Nowack, D. Schlom, D. Ralph, T. Ono, and G. Fuchs, Spin Seebeck Imaging of Spin-Torque Switching in Antiferromagnetic Pt/NiO Heterostructures, *Phys. Rev. X* **9**, 041016 (2019).
- [19] J. Xu, C. Zhou, M. Jia, D. Shi, C. Liu, H. Chen, G. Chen, G. Zhang, Y. Liang, J. Li, W. Zhang, and Y. Wu, Imaging antiferromagnetic domains in nickel oxide thin films by optical birefringence effect, *Phys. Rev. B* **100**, 134413 (2019).
- [20] H. Meer, F. Schreiber, C. Schmitt, R. Ramos, E. Saitoh, O. Gomonay, J. Sinova, L. Baldrati, and M. Kläui, Direct imaging of current-induced antiferromagnetic switching revealing a pure thermomagnetoelastic switching mechanism in NiO, *Nano Lett.* **21**, 114 (2021).
- [21] X. Chen, X. Zhou, R. Cheng, C. Song, J. Zhang, Y. Wu, Y. Ba, H. Li, Y. Sun, Y. You, Y. Zhao, and F. Pan, Electric field control of Néel spin-orbit torque in an antiferromagnet, *Nat. Mater.* **18**, 931 (2019).
- [22] V. Eremenko and N. Kharchenko, Magneto-optics of antiferromagnets, *Phys. Rep.* **155**, 379 (1987).
- [23] X. Chen, *et al.*, Observation of the antiferromagnetic spin Hall effect, *Nat. Mater.* **20**, 800 (2021).
- [24] M. Fiebig, V. V. Pavlov, and R. V. Pisarev, Second-harmonic generation as a tool for studying electronic and magnetic structures of crystals: Review, *J. Opt. Soc. Am. B* **22**, 96 (2005).
- [25] A. Sanger, V. P. M. Bayer, and M. Fiebig, Distribution of antiferromagnetic spin and twin domains in NiO, *Phys. Rev. B* **74**, 144401 (2006).
- [26] H.-M. Hong, Y.-J. Kang, J. Kang, E.-C. Lee, Y.-H. Kim, and K. J. Chang, Effect of chemical bonding on the magnetic stability and magnetic moment in Mn-based binary compounds, *Phys. Rev. B* **72**, 144408 (2005).
- [27] R. Lifshitz, in *Encyclopedia of Condensed Matter Physics*, edited by F. Bassani, G. L. Liedl, and P. Wyder (Elsevier, Oxford, 2005), p. 219.
- [28] J. S. Griffith, *The Theory of Transition Metal Ions* (Cambridge University Press, London, 1971).
- [29] R. Birss, *Symmetry and Magnetism* (North-Holland Pub. Co., Amsterdam, 1966).
- [30] E. König and S. Kremer, Ligand field-spin orbit energy levels in the d⁴ and d⁶ electron configurations of octahedral and tetrahedral symmetry, *Z. für Naturforsch. A* **29**, 31 (1974).
- [31] B. N. Figgis and M. A. Hitchman, *Ligand Field Theory and its Applications* (Wiley-VCH, New York, 1999).
- [32] C. Kittel, *Quantum Theory of Solids* (John Wiley & Sons, Hoboken, NJ, 1963).
- [33] V. Jaccarino, *Nuclear resonance in antiferromagnets, in Magnetism IIA: Statistical Models, Magnetic Symmetry, Hyperfine Interactions, and Metals*, edited by G. T. Rado and H. Suhl (Academic Press, New York, 1965), p. 307.
- [34] J. J. van Loef, Temperature dependence of the sublattice magnetization in the stable magnetic phase and the one-third-power law, *Solid State Commun.* **4**, 625 (1966).